Applied Surface Science 345 (2015) 175–181

Contents lists available at ScienceDirect

Applied Surface Science

journal homepage: www.elsevier.com/locate/apsusc

One-step synthesis of magnetic chitosan polymer composite films

Federico Cesano[a], Gaia Fenoglio[a], Luciano Carlos[b], Roberto Nisticò[a,*]

[a] University of Torino, Department of Chemistry and NIS Research Centre, Via P. Giuria 7, 10125 Torino, Italy
[b] Instituto de Investigación y Desarrollo en Ingeniería de Procesos, Biotecnología y Energías Alternativas, PROBIEN (CONICET-UNCo), Buenos Aires 1400, Neuquén, Argentina

ARTICLE INFO

Article history:
Received 11 September 2014
Received in revised form
11 December 2014
Accepted 19 March 2015
Available online 30 March 2015

Keywords:
Biopolymers
Chitosan films
Iron oxides
Magnetic materials
Magnetic force microscopy

ABSTRACT

In this study, a magnetic iron oxide–chitosan composite film is synthesized by one-step method and thoroughly investigated in order to better understand its inorganic/organic properties. A deep physico-chemical characterization of the magnetic films has been performed. In particular, the material composition was evaluated by means of XRD and ATR-FTIR spectroscopy, whereas the thermal stability and the subsequent inorganic phase transitions involving iron oxide species were followed by TGA analyses carried out at different experimental conditions (i.e. inert and oxidative atmosphere). The magnetic properties of the films were tested at the bulk and at the surface level, performing respectively magnetization hysteresis curve and magnetic force microscopy (MFM) surface mapping. Results indicate that the synthesized material can be prepared through a very simple synthetic procedure and suggests that it can be successfully applied for instance to environmental applications, such as the adsorption of contaminants from solid and liquid media thanks to its pronounced magnetic properties, which favour its recover.

1. Introduction

Magnetic materials consisting of iron oxide particles (typically magnetite and maghemite) dispersed in and/or stabilized by a polymer matrix, have received great attention as a new generation of magnetic stimuli-responsive materials that combine the advantages of both components [1,2]. Such smart inorganic/organic system has been proven to be applicable in many fields, in particular in drug delivery, separation and/or purification of chemicals, development of shape-memory materials and in catalysis [3–6]. In this context, chitosan (a biopolymer derived from chitin, the most abundant natural amino polysaccharide), is a very promising material and has found many applications, such as in the waste water purification from heavy metals and/or dyes [7,8], in marine water bioremediation from oil spills [9], in membrane technologies (water softening process) [10], in the cosmetics industry [11] and as protecting coatings for oxygen-sensible products [12]. Also, according to its antibacterial capacity, chitosan can be used in the biomedical field as biocompatible and bioresorbable material for sutures [13] and as a smart antibacterial coating, for example in abdominal surgery applications [14,15].

There are several chemical species classified under the name of iron oxides. Among the four known Fe_2O_3 phases [16], the α-phase or hematite (a reddish antiferromagnetic material with a trigonal corundum structure) [17] and the γ-phase or maghemite (a black ferrimagnetic material with a spinel crystalline structure) [18] are the most important. Maghemite is an unstable phase and loses its magnetic susceptibility over time [16], even at room temperature (RT). By starting from the most abundant magnetic form (magnetite, Fe_3O_4), a ferrous/ferric oxide mix with a spinel structure, the maghemite can be formed by topotactic oxidation of the magnetite and their interconversion depends on the oxidation and reduction processes. Thus, generalizing, maghemite can be viewed as a ferrous-deficient magnetite isometric crystalline form [19].

According to the water adsorption capacity and the thermal properties of chitosan [20], such amino polysaccharide seems to be a good candidate for the development of magnetic composites based on iron oxide. In fact, electrostatic attraction mechanisms between chitosan macromolecular chains and iron oxide may promote a good dispersion of nanoparticles [21,22]. In particular, the chemistry of chitosan is due to its polar groups (amino and hydroxyl moieties) involved in chelation processes [23] and to the interactions of these species with inorganic particles [21,24].

Many works have been focused on the production of chitosan-stabilized magnetic nanoparticles [1,3,9,25,26], which are protected by the polymer coating, but only few interesting studies have been realized on the synthesis of magnetic chitosan films,

* Corresponding author. Tel.: +39 011 6707533; fax: +39 011 6707855.
E-mail address: roberto.nistico@unito.it (R. Nisticò).

http://dx.doi.org/10.1016/j.apsusc.2015.03.154
0169-4332/

whose potential smart applications in many technological fields are significantly attractive [21,27]. The most widely used method for the synthesis of magnetic chitosan composite (MCC) films consists in dispersing the previously synthesized iron oxide nanoparticles into a chitosan solution and subsequently filming the hybrid organic/inorganic mixture [28–30]. However, since the chitosan solution is quite viscous, there is a high risk of aggregation among the iron oxide nanoparticles due to a not totally homogeneous dispersion in the organic matrix. In this context, this work aims at the in situ preparation of iron oxide by direct co-precipitation method from the chitosan solution as both dispersant and stabilizing matrix in a one-step process. Besides a more simple procedure, the higher uniformity of the magnetic particles dispersion inside the organic matrix can be obtained.

The morphology was evaluated by scanning electron microscopy (SEM) coupled with EDS spectroscopy and by atomic force microscopy in the intermittent-Contact mode (AFM-iC), whereas gas-volumetric N_2 adsorption/desorption experiments were performed for estimating the material porosity. Physico-chemical properties of the chitosan matrix were investigated by means of ATR-FTIR spectroscopy, while the presence of iron oxide particles and the identification of the crystalline phase were carried out by X-ray diffraction (XRD). Moreover, thermo-gravimetric analysis (TGA) was performed in order to evaluate the thermal stability of such material, but also iron oxides phase transitions induced by heating processes (conducted both in inert and oxidative atmosphere). Bulk and surface magnetic properties were assessed by means of magnetization measurement and by magnetic force microscopy (MFM), respectively. Microgravimetric adsorption isotherms of water (polar reference molecule) and toluene (apolar reference molecule) on MCC film were obtained in order to evaluate its adsorption capacity.

2. Experimental

2.1. Reagents and materials

Iron precursors were anhydrous ferric chloride $FeCl_3$ (CAS 7705-08-0, purity ≥98%) and ferrous sulphate heptahydrate $FeSO_4{\cdot}7H_2O$ (CAS 7782-63-0, purity ≥99.5%) both purchased from Fluka Chemika. Partially N-deacetylated chitosan (DD = 75–85%) of medium molecular weight (M_v = 190–310 kDa) with Brookfield viscosity of 200–800 cps (from crab shells, Aldrich, CAS 9012-76-4) was selected as organic dispersant/stabilizing matrix. Ammonium hydroxide solution (CAS 1336-21-6, NH_3 essay 28–30%) was purchased from Aldrich, whereas hydrochloric acid (CAS 7647-01-0, HCl 37 wt.%) was purchased from Fluka Chemika. All chemicals were used without further purification.

2.2. Magnetic film preparation

The magnetic chitosan-based film has been synthesized by means of a modified procedure reported in the literature [31,32] for the synthesis of coated-iron oxide magnetic nanoparticles stabilized by humic substances. Chitosan was used instead of humic substances as dispersant and stabilizing matrix. 3.7 g of $FeCl_3$ and 4.17 g of $FeSO_4{\cdot}7H_2O$ (molar ratio Fe^{3+}/Fe^{2+} = 1.5) were dissolved in 100 ml of deionized water and heated up to 90 °C. Once the temperature was reached, two solutions were added in sequence: (a) 10 ml of 25 vol.% ammonium hydroxide and (b) 50 ml of a previously prepared 1.0 wt.% chitosan solution in weak acid environment to favour the solubilization (2 vol.% HCl). The mixture was mechanically stirred at 90 °C for 30 min and then cooled to room temperature (RT). This way a dispersion of magnetic iron oxide particles in chitosan matrix has been directly obtained in a one-step process. Such black viscous solution was purified by washing twice with water and deposited onto glass Petri dishes until solidification. Finally, the magnetic solid (magnetic chitosan composite, MCC in the following) was oven-dried at 75 °C for 8 h, obtaining a soft and black film with thickness of ca. 3 mm. MCC has been manually crumbled in order to perform the characterization measurements.

2.3. Physico-chemical characterization

Atomic force microscopy measurements were performed in the intermittent-Contact (iC) mode by using a modified Nanosurf Easyscan2 AFM instrument, equipped with a 10 μm scan-head, high performance anti-vibration platform and a shielded and acoustically insulated enclosure. Magnetic force microscopy (MFM) measurements were performed by using the same instrument in a dual-pass mode. The first scan was for the morphological imaging in iC-mode, while the second scan was operated at constant-height (Z) above the same surface with a magnetic probe (Multi75M-G, Budget Sensors; resonant frequency = 75 kHz, force constant = 3 N/m) with a tip radius of about 60 nm by monitoring the shifting of the phase signal [33]. The magnetic tip was magnetized by an external magnet (magnetization along the tip-axis) and tested on a magnetic grid (HDD surface) prior to measurements.

Magnetization measurements were carried out with a LakeShore 7404 vibrating sample magnetometer. The hysteresis loop of the samples was registered at RT as the magnetic field was cycled between −2 and 2 kOe.

Scanning electron microscopy (SEM) analyses were carried out by using a ZEISS EVO 50 XVP microscope with LaB_6 source, equipped with detectors for secondary electron collection and energy dispersive X-ray spectrometry (EDS) probe for elemental analyses. Since samples are insulating, they were covered with a gold layer of ca. 15 nm of thickness before the analysis to avoid any charging effect (Bal-tec SCD050 sputter coater). The presence of gold in EDS spectra (principal signal at ca. 2.2 keV) is due to this step and will not be evidenced in the following data discussion.

N_2 adsorption–desorption experiments were carried out by means of ASAP 2020 instrument (Micromeritics) in order to determine the specific surface area (BET model) [34] and porosity (DFT model) of sample. The density functional theory (DFT) for slit pores at low regularization was applied in order to consider simultaneously micro and mesoporosity [35,36]. The magnetic sample (ca. 1 g) was outgassed at 60 °C for about 48 h in vacuo (residual pressure 10^{-2} mbar) to ensure the complete removal of atmospheric contaminants from the surface before the analysis.

Fourier transform infrared (FTIR) spectra were recorded in attenuated total reflection (ATR) mode (diamond cell for single reflection) in a Bruker Vector 22 spectrophotometer equipped with Globar source, DTGS detector, and working with 512 scans at 4 cm^{-1} of resolution in the range 4000–400 cm^{-1}. ATR spectra were obtained repeating the acquisition for three times.

X-ray diffraction (XRD) patterns were obtained by using a X'Pert PRO MPD diffractometer from PANalytical, in Bragg-Brentano geometry, equipped with Cu anode, ultrafast detector and working at 40 kV and 30 mA, ¼ slit. The acquisition was performed with an interval step of 0.002° with 30 s/step in order to improve the signal to noise ratio. Qualitative analysis of the spectra has been performed with EVA software using ICSD database. XRD patterns have been processed with MAUD software in order to produce quantitative data and collect information on microstructure behaviour. NIST 1976a alumina standard has been used to evaluate the instrumental broadening of the peaks.

Thermo-gravimetric analysis (TGA) was carried out by means of a TA Q600 (TA Instruments). TGA tests were performed in order to monitor the chitosan matrix degradation, the iron oxides phase transitions and quantitative measurements. The thermal analysis

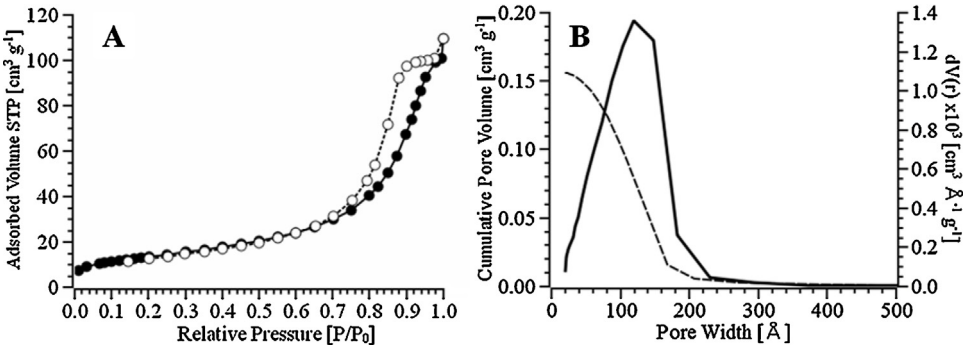

Fig. 1. N_2 adsorption–desorption isotherms at 77 K (A) and DFT pore size distribution (B) of the MCC film. Dark symbols refer to the adsorption branch of the isotherm, empty symbols to the desorption branch.

was performed with a heating ramp of 10 °C/min from RT to 800 °C, both in nitrogen and air. Two replicas were registered for each treatment condition.

Microgravimetric adsorption isotherms were obtained at 24.76 ± 0.04 °C with a microbalance (IGA002 by Hiden), contacting the MCC (ca. 100 mg) outgassed in vacuo at 25 °C with water and toluene vapours [37]. The temperature control was guaranteed by a thermostatic bath.

3. Results and discussion

3.1. Morphological evaluation and magnetic properties determination

Gas-volumetric tests performed on the material allow to evaluate the porosity of the magnetic composite polymer as mesoporous. The isotherm and the DFT pore size distribution curve of the magnetic sample are shown in Fig. 1: the isotherm is of the type IV, with a hysteresis loop of type H2 (from IUPAC classification) in the relative pressure range 0.6–1. The sample has 49 m^2/g of specific BET surface area and 0.16 cm^3/g of mesopore volume (Fig. 1B, dotted line) with a symmetric pore size distribution in the range 5–20 nm centred at 12 nm (Fig. 1B, solid line).

The morphology of MCC film was evaluated by SEM-EDS and AFM analyses. The films present a quite high surface roughness, whereas EDS spectra (not reported for the sake of brevity) confirmed the presence of carbon, oxygen and iron signal elements (SEM image is reported in the Supplementary Material, SM in the following).

Supplementary figures related to this article can be found, in the online version, at http://dx.doi.org/10.1016/j.apsusc.2015.03.154.

In order to evidence the magnetic domain dimensions, a simultaneous morphological and magnetic mapping of the surface was carried out by means of an AFM instrument performing MFM tests.

AFM images of the MCC films are shown in Fig. 2 (unfiltered images are reported in the SM section). The derivative image

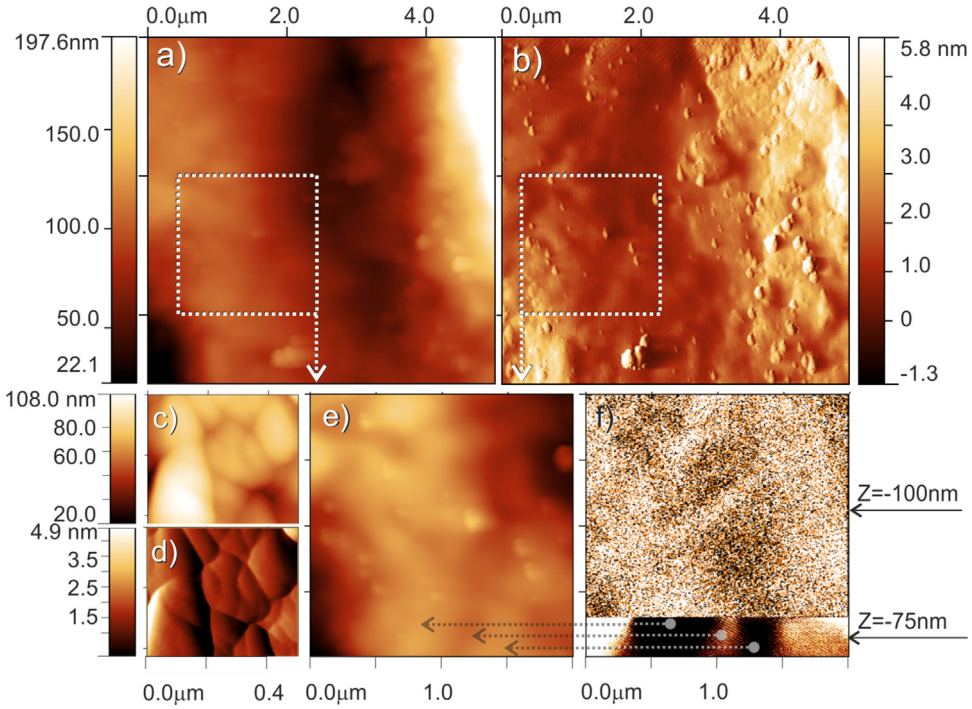

Fig. 2. AFM images of the MCC polymer surface: 5 μm × 5 μm topography (a) and relative 5 μm × 5 μm derivative data (b), 0.5 μm × 0.5 μm high-resolution topography (c) and relative 0.5 μm × 0.5 μm derivative data (d); AFM topography (e) and MFM map (f) of the region selected in (a), respectively. The magnetic properties of the material surface were obtained on flat regions, by minimizing topographic contributions occurring at lower heights (here Z = 75 nm) by working at higher constant-heights above the surface (100 nm > Z > 150 nm), where only magnetic properties (long-range forces) can be detected.

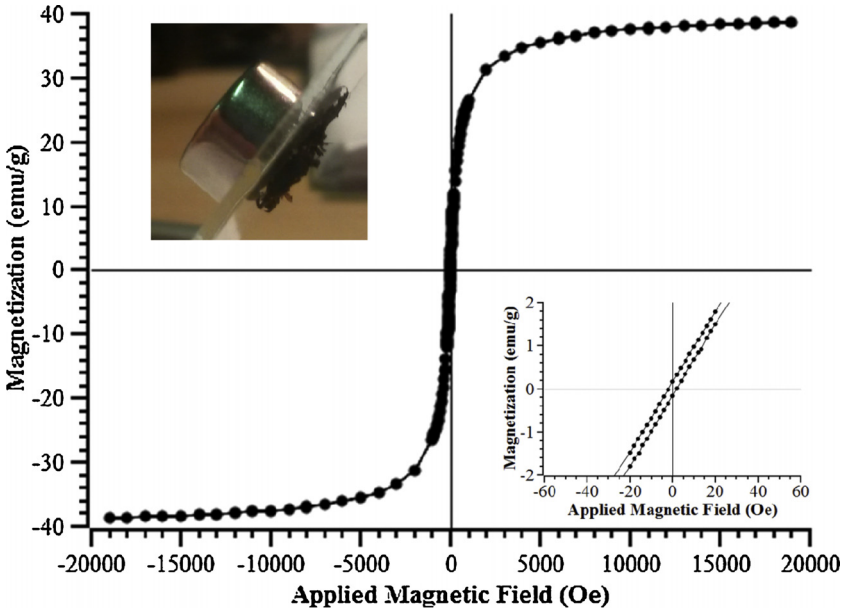

Fig. 3. Magnetization curve for the MCC material. Insets show the magnetization curve enlargement in order to highlight the middle section hysteresis loop (bottom) and a picture showing the magnetic response of the inorganic–organic film versus a commercial neodymium magnet (top).

(obtained as a difference between two consecutive data points) of the topography signal allows to better evidence the roughness of the surface (root-mean-squared roughness = 38 nm, average roughness = 32 nm) [38]. These data are in accordance with the SEM results. At higher resolution (Fig. 2C and D) the surface of the polymer is constituted by agglomerated moieties of rounded shape with dimensions in the 0.1–0.3 μm size range, in agreement with the SEM results [39,40]. The combined morphology/magnetic properties performed on the more regular and flat selected region (Fig. 2A), are shown in Fig. 2E and F, respectively. The topography of this region has been collected in one scan (Fig. 2E), whereas the associated magnetic signal has been obtained at a constant height and sampled in another scan (Fig. 2F). The contribution due to the morphology, which is due to a short-range interaction, is reduced by increasing the distance between the surface and the magnetic probe (measurements height). Some morphological artefacts, produced for measurement height of ca. 75 nm, can be avoided increasing the height to 100–150 nm. In this experimental condition, the topography cannot be examined anymore since image contrast is due to magnetic interactions (long-range forces) between the sample and the magnetic probe. This peculiar contrast completely disappears at higher distance (ca. 250 nm). The contrast of Fig. 2F corresponds to the out-of-plane magnetic domains, whose interaction with the magnetic tip is attractive or repulsive depending on the direction of the magnetic moment (pointing towards the surface or in the opposite direction, respectively). The contrast measured is of irregular shape and size, ranging from ca. 100 nm to ca. 1 μm, thus indicating a magnetic anisotropy of the polymer sample, which is associated with the different aggregation state of the magnetic nanoparticles. Due to the lateral resolution limit given by the curvature of the MFM probe (curvature radius ca. 60 nm), it was not possible to illustrate the behaviours of small and isolated magnetic nanoparticles, but only their irregular aggregation.

The magnetic properties of the MCC film were also investigated with a vibrating sample magnetometer at RT in the applied magnetic field sweeping from −2 to 2 kOe. The hysteresis loop magnetization curve is reported in Fig. 3. The magnetic saturation (M_S) of the magnetic chitosan composite film was 38 emu/g and negligible remainance and coercivity was observed in the magnetic loop (Fig. 3, bottom inset), indicating that MCC polymer films present superparamagnetic properties. Moreover, magnetic single domain state was verified since sample magnetism does not vary across the magnetic probe. Such excellent magnetic properties indicate that the polymer composite possesses strong magnetic response and can be easily recovered by an external magnetic field (Fig. 3, top inset).

3.2. Physico-chemical characterization, thermal behaviour and adsorption capacity

Fig. 4 shows the ATR-FTIR spectra of both MCC films (Section A) and reference chitosan powder (Section B) in the 1200–800 cm^{-1} range. The presence of a wide band centred at 1050 cm^{-1} in the medium infrared range is certainly due to chitosan fingerprint vibrations of both glycosidic and C–O–C groups [14,20]. The composite material presents less resolved components of the 1050 cm^{-1} band with respect to the reference chitosan spectrum,

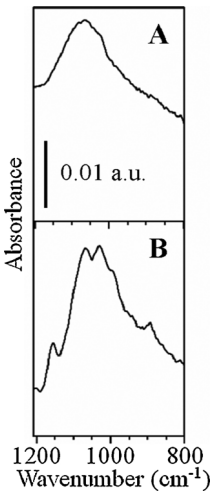

Fig. 4. ATR-FTIR spectra in the 1200–800 cm^{-1} range of the MCC film (A) and of the commercial chitosan powder (B).

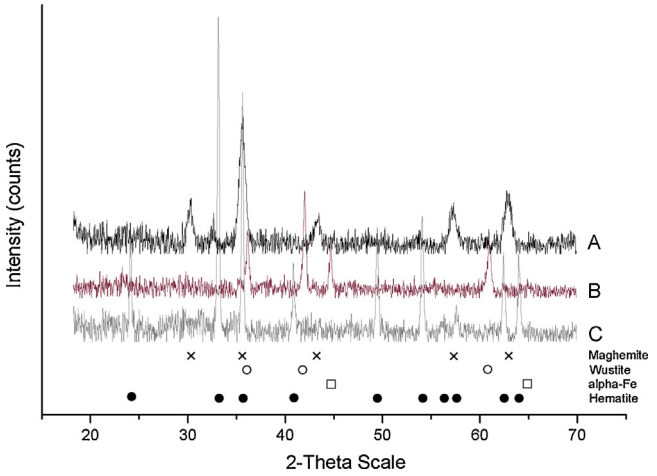

Fig. 5. XRD patterns of the obtained (A), nitrogen-heated (B) and air-heated (C) MCC material. The main reflections due to maghemite (black cross), wüstite (white circle), metal iron alpha-phase (white square) and hematite (black circle) are highlighted and labelled.

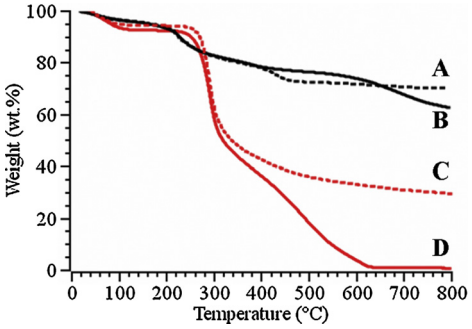

Fig. 6. TG curves of: (i) MCC film heated in nitrogen (black dotted line, curve A) or in air atmosphere (black solid line, curve B); (ii) chitosan reference material heated in nitrogen (red dotted line, curve C) or in air atmosphere (red solid line, curve D). (For interpretation of the references to color in this figure legend, the reader is referred to the web version of this article.)

probably because the complex interactions occurring between chitosan polar groups and iron oxide nanoparticles [39].

The structural characterization of iron oxide particles was carried out by XRD (Fig. 5). No relevant signals are expected from chitosan matrix since its XRD pattern presents only two broad and weak reflections attributable to the amorphous structure with a short-range order [14,20,41–43].

The diffractogram of the sample as prepared (Fig. 5, curve A) presents the characteristic maghemite diffraction pattern of a centred cubic crystalline structure [44] with peaks due to (2 2 0), (3 1 1), (4 0 0), (4 2 2), (5 1 1) and (4 4 0) planes. The position of the peaks is almost coincident with those of the magnetite phase, but the relative intensity of the most intense ones suggests that maghemite is present in this sample. A peak at around $2\theta = 32^\circ$ could be assigned to a small amount of hematite phase, although its position is slightly shifted with respect to the most relevant reflection of hematite.

Quantitative and microstructural information have been obtained performing a Rietveld refinement of the measured curves [45], although the low signal to noise ratio of the diffractograms collected is not optimal for this kind of analysis. Moreover, the dispersion of the crystalline phases in the organic matrix of chitosan and the presence of an amorphous contribution due to the polymer matrix make difficult the background fitting. The strategy adopted to overcome the problems was to consider only the most relevant range of $2\theta = 30–60^\circ$ inducing an ulterior uncertainty of the refinement due to truncation. Therefore, basing on Rietveld theory, the average maghemite crystalline size calculated from the selected range of the diffraction pattern of maghemite species dispersed in the polymer chitosan matrix seemed to be of ca. 18 ± 1 nm diameter. By comparing the XRD results with the previously presented MFM images (Fig. 2), a big difference between the maghemite nanoparticles diameters calculated by Rietveld theory (ca. 20 nm) and the magnetic domain sizes calculated on the basis of the contrast (comprised in the 100 nm–1 μm range size) is obtained. Basing on these results, we can probably assume that the observed magnetic domains are generated by aggregated particles in the polymer matrix and not to single magnetic maghemite particle, although the presence of single and isolated magnetic nanoparticles cannot be excluded.

The thermal behaviours of the MCC polymer film (and in particular the action actuated by the polymer matrix) were studied coupling TGA measurements (carried out both in nitrogen and in air) and XRD, analyzing the structure of materials submitted to thermal analyses. The TGA curves of the material heated in nitrogen (reducing condition) and air (oxidative condition) are reported in Fig. 6, together with the curves of the reference chitosan.

Chitosan presents two main degradation steps, the first one due to water evaporation at temperature lower than 100 °C and the second one at ca. 300 °C due to the polysaccharide degradation (a more detailed investigation of chitosan thermal degradation behaviour in a nitrogen atmosphere is thoroughly discussed in [20]). In nitrogen atmosphere (i.e. reducing condition), chitosan leaves at 800 °C a graphitic residue of ca. 30 wt.% (Fig. 6, curve C), whereas in air (i.e. oxidative condition) only a negligible residue (less than 1 wt.%) was obtained at ca. 600 °C (Fig. 6, curve D) because of the almost complete combustion caused by the presence of oxygen.

The thermal degradation of the MCC material follows the trend of the chitosan polymer matrix showing the most relevant degradation/oxidation steps of the polymer. The 70 wt.% residue is black and magnet-sensitive, but the relative diffraction pattern (Fig. 6, curve B) presents the characteristic wüstite signals (FeO, 84 ± 5 wt.%) with peaks due to (3 3 3), (6 0 0) and (6 6 0) planes, together with (1 1 0) and (2 0 0) planes due to metallic iron (15 ± 8 wt.%), whereas no detectable peaks due to magnetic phases are visible in the diffractogram of the more reduced iron oxide form, with a real composition close to $Fe_{0.90}O$ [46]. The ca. 63 wt.% residue of the MCC material thermally treated in air (i.e. oxidative atmosphere) is not magnetic anymore and presents itself as a reddish solid (Fig. 5, curve A). The XRD pattern of this residue is reported in Fig. 6, curve C, and presents the characteristic hematite trigonal crystalline structure pattern of diffraction, with signals due to (1 0 4), (1 1 0), (0 0 6), (1 1 3), (2 0 2), (0 2 4), (1 1 6), (2 1 1), (1 2 2), (0 1 8), (2 1 4) and (3 0 0) hematite planes [47].

According to the results obtained, the hypothesized reactions of the material are reported in Scheme 1. It is possible to assume that the reducing atmosphere induces a first reduction of the maghemite (γ-Fe_2O_3) into the wüstite form (FeO), thanks to the graphitic carbon produced by chitosan (Eq. (1)); subsequently, since wüstite is thermodynamically unstable above 575 °C, at this temperature, FeO can disproportionate into metal iron (Fe) and

In nitrogen atmosphere:

$\gamma\text{-}Fe_2O_3 + C \rightarrow 2FeO + CO\uparrow$ (1)

$4\,FeO \rightarrow Fe + Fe_3O_4$ (2)

$Fe_3O_4 + C \rightarrow 3\,FeO + CO\uparrow$ (3)

In air atmosphere:

$\gamma\text{-}Fe_2O_3 \rightarrow \alpha\text{-}Fe_2O_3$ (4)

Scheme 1. Thermally induced reduction/oxidation reactions involving iron oxides in different chemical environments (reductive vs. oxidant atmosphere).

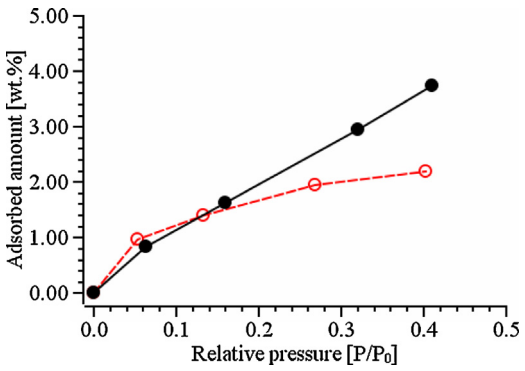

Fig. 7. Microgravimetric adsorption isotherms of water (black solid line) and toluene (red dashed line) vapours on MCC film activated at 25 °C. Adsorption experiments were carried out at 25 °C.

magnetite (Fe_3O_4) (Eq. (2)); in the presence of carbon, also magnetite evolves into wüstite (Eqs. (2) and (3)) except small amounts (the heated sample is still magnetic) protected by a carbon coating and not detectable by XRD.

Otherwise, the oxidative atmosphere induces the complete oxidation of chitosan and its removal as H_2O and CO_2, with the consequent formation of the stable hematite phase (α-Fe_2O_3) (Eq. (4)) for temperature as high as 600 °C [17,48].

In addition, the quantity of the inorganic and of the polymer phases of the native composite material can be estimated. In fact, considering the weight differences of the residues of the pure chitosan (negligible) and of the MCC material treated in air (ca. 60 wt.%), the obtained iron oxide/polymer weight ratio is ca. 3/2.

In order to evaluate the adsorption capacity of MCC film, microgravimetric adsorption experiments of water (polar reference molecule) and toluene (apolar reference molecule) vapours on the magnetic film surface have been performed and adsorption isotherms are reported in Fig. 7. Only adsorption profiles in the relative pressure range between 0 and $0.5P/P_0$ were discussed, in order to consider only the interaction of adsorbates with the surface and avoid the capillary condensation due to the porosity of the material. According to the experimental curves observed, the adsorbing properties of the system are not so important with respect to other more active materials, nevertheless they are significant. Moreover, calculating the adsorbed amounts as a function of the chitosan fraction, the coverage at $0.4P/P_0$ increase to ca. 5.5 wt.% for toluene and ca. 9 wt.% for water vapour. The water vapour adsorption trend confirms the hydrophilic character of the MCC film surface (i.e. water adsorbed amount is twice the toluene coverage), thus suggesting that it is of potential application as material for adsorbing polar pollutants. This is an important issue that deserves future research.

4. Conclusions

A simple method for the synthesis of magnetic composite polymer material was proposed.

Magnetic properties of the polymer composite material have been evaluated by means of magnetization hysteresis curve and MFM surface analysis. Both techniques suggested that such material presents at room temperature superparamagnetic properties, extensive and homogeneously distributed magnetic response, with domain size comprises between 100 nm and 1 μm. This way, it seemed that magnetic domains have been generated by aggregates of maghemite particles inside the chitosan matrix and FTIR spectroscopy suggests a strong interaction existing between iron oxide particles and polymer matrix.

The thermal stability of the magnetic composite polymer has been investigated and different behaviours have been observed after thermal treatment in reducing or oxidative atmosphere: a reaction mechanism considering the modification of the iron oxide has been proposed.

In general, the magnetic composite polymer material presents a great potential for application in many industrial processes, nanotechnology, and/or other technological fields thanks to the well known chitosan properties and for its magnetic response.

Acknowledgments

The authors would like to thank Dr. A. Agostino, Mr. A. Allera and Ms. F. Franzoso (University of Torino, Italy) for technical assistance, Prof. D. Scarano and Dr. G. Magnacca (University of Torino, Italy) for the precious help in the data elaboration and Dr. M.G. Faga (CNR-IMAMOTER, Italy) for SEM-EDS measurements.

References

[1] Y. Li, D. Yuan, M. Dong, Z. Chai, G. Fu, Facile and green synthesis of core–shell structured magnetic chitosan submicrospheres and their surface functionalization, Langmuir 29 (2013) 11770–11778.
[2] T. Nardi, M. Sangermano, Y. Leterrier, P. Allia, P. Tiberto, J.-A.E. Månson, UV-cured transparent magnetic polymer nanocomposites, Polymer 54 (2013) 4472–4479.
[3] W. Zhang, S. Jia, Q. Wu, S. Wu, J. Ran, Y. Liu, J. Hou, Studies of the magnetic field intensity on the synthesis of chitosan-coated magnetite nanocomposites by co-precipitation method, Mater. Sci. Eng. C 32 (2012) 381–384.
[4] D.K. Yi, S.S. Lee, J.Y. Ying, Synthesis and applications of magnetic nanocomposite catalysts, Chem. Mater. 18 (2006) 2459–2461.
[5] J.K. Oh, J.M. Park, Iron oxide-based superparamagnetic polymeric nanomaterials: design, preparation, and biomedical application, Prog. Polym. Sci. 36 (2011) 168–189.
[6] A.M. Schmidt, Electromagnetic activation of shape memory polymer networks containing magnetic nanoparticles, Macromol. Rapid Commun. 27 (2006) 1168–1172.
[7] Y. Vijaya, S.R. Popuri, V.M. Boddu, A. Krishnaiah, Modified chitosan and calcium alginate biopolymer sorbents for removal of nickel(II) through adsorption, Carbohydr. Polym. 72 (2008) 261–271.
[8] W.S. Wan Ngah, L.C. Teong, M.A.K.M. Hanafiah, Adsorption of dyes and heavy metal ions by chitosan composites: a review, Carbohydr. Polym. 83 (2011) 1446–1456.
[9] S. Babel, T.A. Kurniawan, Low-cost adsorbents for heavy metals uptake from contaminated water: a review, J. Hazard. Mater. 97 (2003) 219–243.
[10] S. Ladet, L. David, A. Domard, Multi-membrane hydrogel, Nature 452 (2008) 76–79.
[11] M. Rinaudo, Chitin and chitosan: properties and applications, Prog. Polym. Sci. 31 (2006) 603–632.
[12] A.B. Falcon, J.C. Cabrera, D. Costales, M.A. Ramirez, G. Cabrera, V. Toledo, M.A. Martinez-Tellez, The effect of size and acetylation degree of chitosan derivatives on tobacco plant protection against *Phytophthora parasitica nicotianae*, World J. Microbiol. Biotechnol. 24 (2008) 103–112.
[13] E.I. Rabea, M.E.T. Badawy, C.V. Stevens, G. Smagghe, W. Steurbaut, Chitosan as antimicrobial agent: applications and mode of action, Biomacromolecules 4 (2003) 1457–1465.
[14] R. Nisticò, M.G. Faga, G. Gautier, G. Magnacca, D. D'Angelo, E. Ciancio, G. Piacenza, R. Lamberti, S. Martorana, Physico-chemical characterization of functionalized polypropylenic fibers for prosthetic applications, Appl. Surf. Sci. 258 (2012) 7889–7896.
[15] P. Avetta, R. Nisticò, M.G. Faga, D. D'Angelo, E. Aimo Boot, R. Lamberti, S. Martorana, P. Calza, D. Fabbri, G. Magnacca, Hernia-repair prosthetic devices functionalised with chitosan and ciprofloxacin coating: controlled release and antibacterial activity, J. Mater. Chem. B 2 (2014) 5287–5294.
[16] R. Dronskowski, The little maghemite story: a classical functional material, Adv. Funct. Mater. 11 (2001) 27–29.
[17] I.V. Chernyshova, M.F. Hochella Jr., A.S. Maddenc, Size-dependent structural transformations of hematite nanoparticles. 1. Phase transition, Phys. Chem. Chem. Phys. 9 (2007) 1736–1750.
[18] D.L.A. de Faria, S. Venâcio Silva, M.T. de Oliveira, Raman microspectroscopy of some iron oxides and oxyhydroxides, J. Raman Spectrosc. 28 (1997) 873–878.
[19] R.M. Cornell, U. Schwertmann, The Iron Oxides: Structure, Properties, Reactions, Occurrences and Uses, Wiley-VCH, Weinheim, Germany, 2003.
[20] I. Corazzari, R. Nisticò, F. Turci, M.G. Faga, F. Franzoso, S. Tabasso, G. Magnacca, Advanced physico-chemical characterization of chitosan by means of TGA coupled on-line with FTIR and GCMS: thermal degradation and water adsorption capacity, Polym. Degrad. Stab. 112 (2015) 1–9.
[21] J.B. Marroquin, K.Y. Rhee, S.J. Park, Chitosan nanocomposite films: enhanced electrical conductivity, thermal stability, and mechanical properties, Carbohydr. Polym. 92 (2013) 1783–1791.

[22] A. Zhu, L. Yuan, T. Liao, Suspension of Fe_3O_4 nanoparticles stabilized by chitosan and o-carboxymethylchitosan, Int. J. Pharm. 350 (2008) 361–368.
[23] K. Sreenivasan, Thermal stability studies of some chitosan–metal ion complexes using differential scanning calorimetry, Polym. Degrad. Stab. 52 (1996) 85–87.
[24] S. Wang, L. Shen, W. Zhang, Y. Tong, Preparation and mechanical properties of chitosan/carbon nanotubes composites, Biomacromolecules 6 (2005) 3067–3072.
[25] X. Liu, Q. Hu, Z. Fang, X. Zhang, B. Zhang, Magnetic chitosan nanocomposites: a useful recyclable tool for heavy metal ion removal, Langmuir 25 (2009) 3–8.
[26] K. Pospiskova, I. Safarik, Low-cost, easy-to-prepare magnetic chitosan microparticles for enzymes immobilization, Carbohydr. Polym. 96 (2013) 545–548.
[27] M.A. Garza-Navarro, V. Gonzalez, M. Hinojasa, A. Torres-Castro, Preparation of chitosan/magnetite polymeric-magnetic films, Rev. Mex. Fis. 57 (2011) 51–56.
[28] A. Kaushik, R. Khan, P.R. Solanki, P. Pandey, J. Alam, S. Ahmad, B.D. Malhotra, Iron oxide nanoparticles-chitosan composite based glucose biosensor, Biosens. Bioelectron. 24 (2008) 676–683.
[29] R. Jiang, Y.-Q. Fu, H.-Y. Zhu, J. Yao, L. Xiao, Removal of methyl orange from aqueous solutions by magnetic maghemite/chitosan nanocomposite films: adsorption kinetics and equilibrium, J. Appl. Polym. Sci. 125 (2012) E540–E549.
[30] S.-F. Wang, Y.-M. Tan, A novel amperometric immunosensor based on Fe_3O_4 magnetic nanoparticles/chitosan composite film for determination of ferritin, Anal. Bioanal. Chem. 387 (2007) 703–708.
[31] L. Carlos, M. Cipollone, D.B. Soria, M.S. Moreno, O.R. Ogilby, F.S. García Einschlag, D.O. Mártire, The effect of humic acid binding to magnetite nanoparticles on the photogeneration of reactive oxygen species, Sep. Purif. Technol. 91 (2012) 23–29.
[32] G. Magnacca, A. Allera, E. Montoneri, L. Celi, D.E. Benito, L.G. Gagliardi, M.C. Gonzalez, D.O. Mártire, L. Carlos, Novel magnetite nanoparticles coated with waste-sourced biobased substances as sustainable and renewable adsorbing materials, ACS Sustain. Chem. Eng. 2 (2014) 1518–1524.
[33] A. Schwarz, M. Bode, R. Wiesendanger, Scanning probe techniques: MFM and SP-STM, in: H. Kronmüller, S.S.P. Parkin (Eds.), Handbook of Magnetism and Advanced Magnetic Materials, vol. 3, Wiley-VCH, Amsterdam, 2006.
[34] S. Brunauer, P.H. Emmett, E. Teller, Adsorption of gases in multimolecular layers, J. Am. Chem. Soc. 60 (1938) 309–319.
[35] D.L. Ou, P.D. Chevalier, I.A. Mackinnon, K. Eguchi, R. Boisvert, K. Su, Preparation of microporous ORMOSILs by thermal degradation of organically modified siloxane resin, J. Sol–Gel Sci. Technol. 26 (2003) 407–412.
[36] R. Nisticò, D. Scalarone, G. Magnacca, Preparation and physico-chemical characterization of large-mesopore silica thin films templated by block copolymers for membrane technology, Microporous Mesoporous Mater. 190 (2014) 208–214.
[37] A. Molinari, G. Magnacca, G. Papazzoni, A. Maldotti, Hydrophobic $W_{10}O_{32}^{4-}$/silica photocatalyst for toluene oxidation in water system, Appl. Catal. B: Environ. 138–139 (2013) 446–452.
[38] M.J. Uddin, F. Cesano, S. Bertarione, F. Bonino, S. Bordiga, D. Scarano, A. Zecchina, Tailoring the activity of Ti-based photocatalysts by playing with surface morphology and silver doping, J. Photochem. Photobiol. A 196 (2008) 165–173.
[39] B.G. Assis, R. Bernardes-Filho, D.C. Vieira, S.P. Campana-Filho, AFM characterization of chitosan self-assembled films, Int. J. Polym. Mater. 51 (2002) 633–638.
[40] W.H. Nosal, D.W. Thompson, L. Yan, S. Sarkar, A. Subramanian, J.A. Woollam, UV–vis-infrared optical and AFM study of spin-cast chitosan films, Colloids Surf. B 43 (2005) 131–137.
[41] K.M. Gregorio-Jauregui, M.G. Pineda, J.E. Rivera-Salinas, G. Hurtado, H. Saade, J.L. Martinez, A. Ilyina, R.G. Lopez, One-step method for preparation of magnetic nanoparticles coated with chitosan, J. Nanomater. (2012), http://dx.doi.org/10.1155/2012/813958.
[42] M.K. Jang, B.G. Kong, Y.I. Jeong, C.H. Lee, J.W. Nah, Physicochemical characterization of alpha-chitin, beta-chitin and gamma-chitin separated from natural resources, J. Polym. Sci. A: Polym. Chem. 42 (2004) 3423–3432.
[43] Y. Saito, H. Kumagai, M. Wada, S. Kuga, Thermally reversible hydration of α-chitin, Biomacromolecules 3 (2002) 407–410.
[44] B. Wang, Q. Kong, F. Quan, Q. Li, Y. Xia, Preparation of nanostructured porous carbon composite fibers from ferrum alginate fibers, J. Appl. Polym. Sci. 128 (2013) 2216–2223.
[45] H.M. Rietveld, A profile refinement method for nuclear and magnetic structures, J. Appl. Crystallogr. 2 (1969) 65–71.
[46] N. Mahmed, O. Heczko, A. Lancok, S.-P. Hannula, The magnetic and oxidation behaviour of bare and silica-coated iron oxide nanoparticles synthesized by reverse co-precipitation of ferrous ion (Fe^{2+}) in ambient atmosphere, J. Magn. Magn. Mater. 353 (2014) 15–22.
[47] D. Mamula-Tartalja, L. Vulicevic, I. Radisavljevic, M. Mitric, V. Andric, B. Kuzmanovic, M. Medic, N. Ivanovic, Effects of manufacturing conditions and heating on properties of electrochemically produced magnetite nano-powders, Ceram. Int. 40 (2014) 3517–3525.
[48] H. Lepp, Stages in the oxidation of magnetite, Am. Mineral. 42 (1957) 679–681.